MoS$_2$ Phototransistor Sensitized by Colloidal Semiconductor Quantum Wells

Huseyin Sar, Nima Taghipour, Ibrahim Wonge Lisheshar, Savas Delikanli, Mustafa Demirtaş, Hilmi Volkan Demir,* Feridun Ay,* and Nihan Kosku Perkgöz*

A phototransistor built by the assembly of 2D colloidal semiconductor quantum wells (CQWs) on a single layer of 2D transition metal dichalcogenide (TMD) is displayed. This hybrid device architecture exhibits high efficiency in Förster resonance energy transfer (FRET) enabling superior performance in terms of photoresponsivity and detectivity. Here, a thin film of CdSe/CdS CQWs acts as a sensitizer layer on top of the MoS$_2$ monolayer based field-effect transistor, where this CQWs–MoS$_2$ structure allows for strong light absorption in CQWs in the operating spectral region and strong dipole-to-dipole coupling between MoS$_2$ and CQWs resulting in enhanced photoresponsivity of one order of magnitude (11-fold) at maximum gate voltage (V_{BG} = 2 V) and two orders of magnitude ($\approx 5 \times 10^2$) at V_{BG} = −1.5 V, and tenfold enhanced specific detectivity. The illumination power-dependent characterization of this hybrid device reveals that the thin layer of CQWs dominates the photogating mechanism compared to the photoconductivity effect on detection performance. Such hybrid designs hold great promise for 2D-material based photodetectors to reach high performance and find use in optoelectronic applications.

1. Introduction

The emerging 2D materials have attracted great attention in the last decade owing to their superior optical[1] and electronic[2] properties giving inspiration for novel devices in electronics and optoelectronics. These 2D materials have been widely studied for a large number of applications including photodetectors,[3] DNA sensors,[4] and catalysts.[5] Among them, layered transition metal dichalcogenide (TMD) semiconductors (e.g., MoS$_2$ and WS$_2$) are particularly of importance with their direct electronic band gaps in their monolayer form and very high ON/OFF contrast ratios when used as active regions in transistors. TMDs demonstrate strong light-matter interaction accompanied with large excitonic binding energy and strong oscillator strength.[6] In addition, the tunable bandgaps of these materials using an external electric field[7] and mechanical strain[8] and their gate voltage dependent photoresponsivity make them promising material platforms for photodetectors[9,10] and photovoltaics.[11] In particular, a single layer of MoS$_2$ exhibits an absorption coefficient of $\alpha = 1 - 1.5 \times 10^6$ cm^{-1}, which results in absorption of approximately 10% of the normal incident light at the excitonic features ($\approx$ 620 and 670 nm).[1,12]

In addition to 2D TMDs, colloidal nanoplatelets (NPLs), alternatively commonly known as colloidal semiconductor quantum wells (CQWs), consist of a quasi-2D structure of atomically-flat semiconductor nanocrystals.[13] Owing to their tight quantum confinement in the vertical direction, CQWs exhibit favorable optical properties including narrow photoluminescence (PL) emission spectra,[14,15] large absorption cross-sections[15–17] and giant oscillator strengths.[16,17] These attractive properties make them versatile and promising candidates in light-generating[16,18] and harvesting[19] applications.

Although MoS$_2$-based phototransistors exhibit high responsivity performance, in the order of $\approx 10^4$AW^{-1}, at low excitation intensities,[20–22] their photodetection performance is hindered by the limited optical absorption of incident light as a result of the ultrathin thickness of 2D TMD semiconductors. To address this issue, various efforts have previously been conducted including surface interface engineering[23] and combining these materials with a light absorber layer.[22,24–30] The latter approach allows for enhancement in the photocurrent generation level via charge transfer or non-radiative energy transfer (NRET) mechanisms. To date, a variety of absorber layer has been used including p-type MoS$_2$,[31] organic dyes,[24] ZnO,[25] graphene,[27,32,33] WS$_2$,[30] and colloidal quantum dots (CQDs).[29,30] However, to the best of our knowledge, the integration of

Dr. H. Sar, I. W. Lisheshar, Dr. M. Demirtaş, Prof. F. Ay,
Prof. N. Kosku Perkgöz
Department of Electrical and Electronics Engineering
Eskisehir Technical University
Eskisehir 26555, Turkey
E-mail: feridunay@eskisehir.edu.tr; nkperkgoz@eskisehir.edu.tr

N. Taghipour, Dr. S. Delikanli, Prof. H. V. Demir
Department of Electrical and Electronics Engineering
Department of Physics
UNAM-Institute of Materials Science and Nanotechnology
Bilkent University
Ankara 06800, Turkey
E-mail: volkan@stanfordalumni.org

Prof. H. V. Demir
Luminous! Centre of Excellence for Semiconductor Lighting and Displays
School of Electrical and Electronic Engineering
School of Physical and Mathematical Sciences
School of Materials Science and Engineering
Nanyang Technological University
Singapore 639798, Singapore

2001198 (1 of 9)

quasi-2D CQWs with 2D-MoS$_2$ monolayer (CQWs-MoS$_2$) has not been considered, among colloids for this purpose although this combination would offer a very favorable solution among colloidal options owing to their matching atomically-flat geometries, and their hybrid structure would thus enable very strong layer-to-layer dipole-dipole coupling.[34] One would rationalize this strategy therefore to achieve substantial photocurrent enhancement compared to any other possible hybrids studied up to present.[34]

A form of NRET interaction, Förster-type resonance energy transfer (FRET) is a near-field electromagnetic dipole-dipole coupling process where an oscillating dipole in the donor species induces a dipole in the acceptor species,[35] and the excitation energy of the donors is non-radiatively transferred to the acceptors.[34] The efficiency and hence the rate of FRET process essentially depends on the distance between acceptor and donor pairs, the spectral overlap between the donor PL emission and the acceptor absorption spectra and combination of dimensionality of the donor[34] and acceptor.[35–37] The potential effectiveness of the FRET on light-harvesting and -detecting applications has been shown previously. For instance, our team previously reported near-unity efficiency of FRET from CdSe/CdS core/crown CQWs to the single-layer of MoS$_2$ (99.88%),[34] accompanied by an ultrafast transfer rate of ≈268 ns^{-1}. This study is an obvious indicator of the promising potential of CdSe/CdS-MoS$_2$ system, or more generally the CQWs-TMD hybrids in photodetection/sensing applications.

In the present study, different from the previously reported ones of our group or others, we show considerable FRET-assisted enhancement in photodetection performance of MoS$_2$ phototransistors sensitized by CQWs. Here, as a model system, we employed a thin film of CdSe/CdS core/crown CQWs as a sensitizer layer directly on top of a MoS$_2$ single layer and systematically studied the photodetection performance of the hybrid system. By exploiting these CdSe/CdS CQW sensitizers interfacing MoS$_2$, we obtain ≈11-fold at V_{BG} = 2.0 V and ≈5 × 10^2-fold at V_{BG} = −1.5 V of enhancement in the photoresponsivity and tenfold in the specific Detectivity (D^*) under the irradiation of 1 μW compared to control group when only bare MoS$_2$ is used. The mechanism responsible for this photoresponsivity enhancement is revealed to be mainly the FRET process by systematically performing time-resolved fluorescence (TRF) spectroscopy and electronic transport measurements of the devices under dark and illuminated conditions. Here we find at a FRET efficiency level of 97.84% and a rate of 21.26 ns^{-1}. An ultra-efficient transfer of excitons from CQWs to monolayer of MoS$_2$. To better understand the underlying mechanism enabling the photocurrent enhancement and the role of FRET in the process, systematical illumination of power-dependent transport measurements and analysis were also performed, as a result of which we found that the energy transfer from CQWs to MoS$_2$ layer is also further coupled into the traps states of MoS$_2$ and leads to an increased effect of photogating.

2. Results and Discussion

Figure 1a depicts a schematic illustration of the CdSe/CdS-MoS$_2$ (CQWs-TMD) hybrid phototransistor. Herein, at the bottom layer, a single layer of MoS$_2$ flakes were grown on a standard microscope coverslip glass substrate with very high monolayer coverage by chemical vapor deposition (CVD) method (Figure S1, Supporting Information).[38] Then, the MoS$_2$ flakes on the glass substrate were transferred to Al$_2$O$_3$/Si substrate through an etching-free, wet transfer method. Having chosen as high-κ dielectric gate oxide material, a thin film layer of Al$_2$O$_3$ (≈44 nm) was deposited on top of Si wafer via atomic layer deposition (ALD) technique (See Supporting Information for details on the device fabrication). The optical microscopy image of the fabricated phototransistor along with its source and drain contacts is shown in Figure 1b. As can be seen in Figure 1b, the channel width of the device is 8 μm. To verify the single layer formation of MoS$_2$ triangle flakes before and after the transfer process, we used μ-Raman and photoluminescence (PL) spectroscopies. The Raman spectra of MoS$_2$ flakes on the glass (before the transfer) and Al$_2$O$_3$/Si (after the transfer) and the deconvoluted Raman modes (E$^1_{2g}$ and A$_{1g}$) using Lorentzian curves are depicted in Figure 1c. The difference between E$^1_{2g}$ and A$_{1g}$ Raman mode positions of MoS$_2$ was employed to determine the thickness of the grown layer, which was found to be 19.3±0.4 and 18.5±0.4 cm^{-1} for the cases before and after the transfer of samples, respectively, indicating monolayer MoS$_2$ flakes in both cases.[39] Typical room-temperature PL spectra obtained from monolayer MoS$_2$[40] on the glass (Figure 1d) and Al$_2$O$_3$/Si (Figure 1e) are deconvoluted to the known excitonic features of MoS$_2$, A- and B-exciton and A-trion peaks, by fitting Gaussian curves.[41] The center wavelengths of A-exciton, B-exciton, and A-trion are found as ≈676, 632 and 697 nm for our MoS$_2$ on its grown substrate (glass) and ≈678, 642, and 691 nm for the transferred MoS$_2$ on the Al$_2$O$_3$/Si substrate, correspondingly. Here, as shown in Figure 1e, the A-trion intensity is slightly increased after the transfer procedure, which can be attributed to the defects introduced unintentionally during the transfer procedure, as the PL characteristics of MoS$_2$ are very sensitive to the doping levels and defect densities. Particularly, the integrated intensity ratio of A-trion ($I_{A-trion}$) to A-exciton ($I_{A-exciton}$) emission is informative about the defect densities, which is based on the mass action law due to the relationship between the charge carrier density and the quasi-particle concentration.[42] In addition, due to the induced defects in the transfer procedure, the center wavelength of the A-trion peak is blue-shifted while no significant intensity variation or peak emission wavelength shift was observed for the A-exciton.[42]

The physical dimensions of CQWs are analyzed by the high-angle annular dark-field transmission electron microscopy (HAADF-TEM) images. In Figure 1f, HAADF-TEM image of the synthesized CQWs is presented and the average width and length of nanocrystals are estimated to be 13.99 ±1.83 and 16.76 ± 2.77 nm, respectively. Subsequently, a dilute dispersion of CdSe/CdS core/crown CQWs (0.15 mg mL^{-1} CQWs/toluene mixed in 0.1% toluene/PMMA host) was uniformly spin-coated onto the fabricated devices (See Supporting Information for the details on the CQWs). The resulting thin film of these CdSe/CdS CQWs acts as an efficient layer of exciton donors, while the monolayer of MoS$_2$ at the bottom layer serves as an exciton sink layer. Figure 1g shows the spectral overlap between the PL spectrum of the donor (CdSe/CdS core/crown CQWs) and the absorption spectrum of the acceptor (MoS$_2$, TMD).

ADVANCED
SCIENCE NEWS
www.advancedsciencenews.com

ADVANCED
OPTICAL
MATERIALS
www.advopticalmat.de
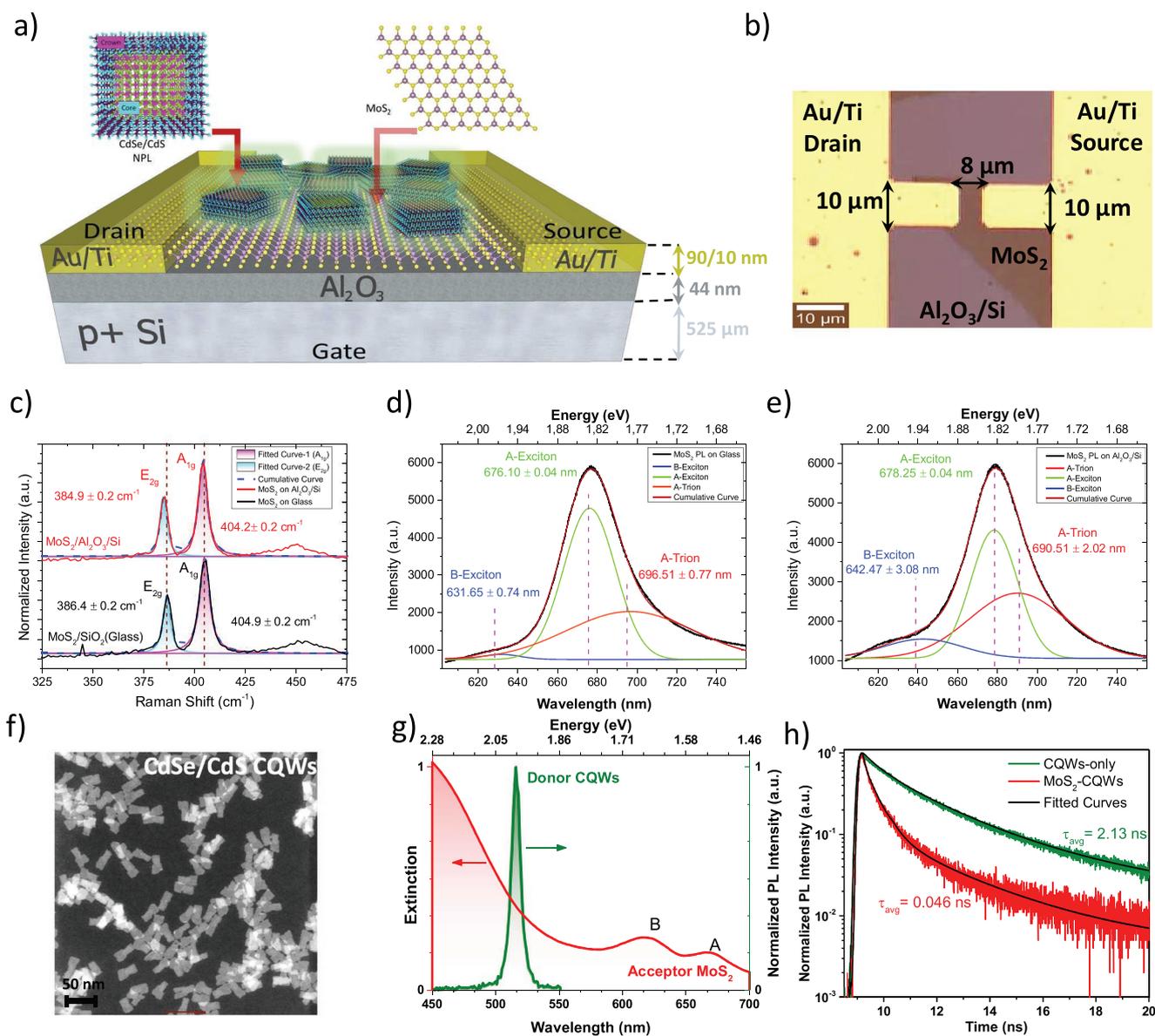
Figure 1. a) Schematic illustration of the proposed CQWs-MoS$_2$ hybrid phototransistor (not drawn to scale). b) Top-view optical microscopy image of the fabricated device along with Au/Ti metal contacts (scale bar is 10 μm). c) Raman spectra of the as-grown MoS$_2$ monolayer on a glass substrate and that after transferred onto Al$_2$O$_3$/Si substrate is shown along with their deconvoluted Raman modes. d) Photoluminescence spectra of MoS$_2$ on glass and e) on Al$_2$O$_3$/Si with their excitonic species: A- and B-excitons and A-trion. f) High-angle annular dark-field transmission electron microscopy image of the CQWs (scale bar is 50 nm). g) Normalized photoluminescence spectrum of the as-synthesized 4 monolayer (ML) thick CdSe/CdS core/crown CQWs (donor) and the overlapping UV–vis absorption spectrum of the MoS$_2$ triangular monolayer flakes (acceptor). h) Photoluminescence decay curves of the solid films of the CQWs-MoS$_2$ assembly and CQWs-only. The solid black lines represent the fitted curves.

The peak emission wavelength of CQWs is at 518 nm with an ultranarrow full-width half maximum of 8 nm at room temperature and the excitonic features of MoS$_2$, the B-exciton and A-exciton peaks, are around 630 and 670 nm, respectively, observable on the absorption profile. To investigate the luminescence characteristics of CQWs in the hybrid of CdSe/CdS-MoS$_2$ (CQWs-TMD, donor–acceptor pair), we employed time-resolved fluorescence (TRF) spectroscopy. To do so, we recorded the PL decay curves of the donor band-edge emission (at 518 nm) for different cases which are shown together in Figure 1h. Here, the CQWs-only sample, in which CQWs

(0.15 mg mL^{-1} CQWs/hexane diluted in 0.1% hexane/PMMA) were deposited on a pre-cleaned quartz substrate, acts as a reference sample for which the amplitude-averaged PL lifetime corresponds to 2.13 ns. As shown in Figure 1h, in the presence of monolayer of MoS$_2$ (i.e., acceptor), however, the PL decay kinetics of donor in the CQWs on MoS$_2$ sample is significantly accelerated and the PL lifetime is reduced to 46 ps, suggesting the opening of a new channel for the relaxation of the carriers in CQWs. This significant decrease in the PL lifetime can be ascribed to FRET or charge transfer process.[34] However, in our structure, the charge transfer is ineffective owing to passivation

ADVANCED
SCIENCE NEWS
www.advancedsciencenews.com

ADVANCED
OPTICAL
MATERIALS
www.advopticalmat.de
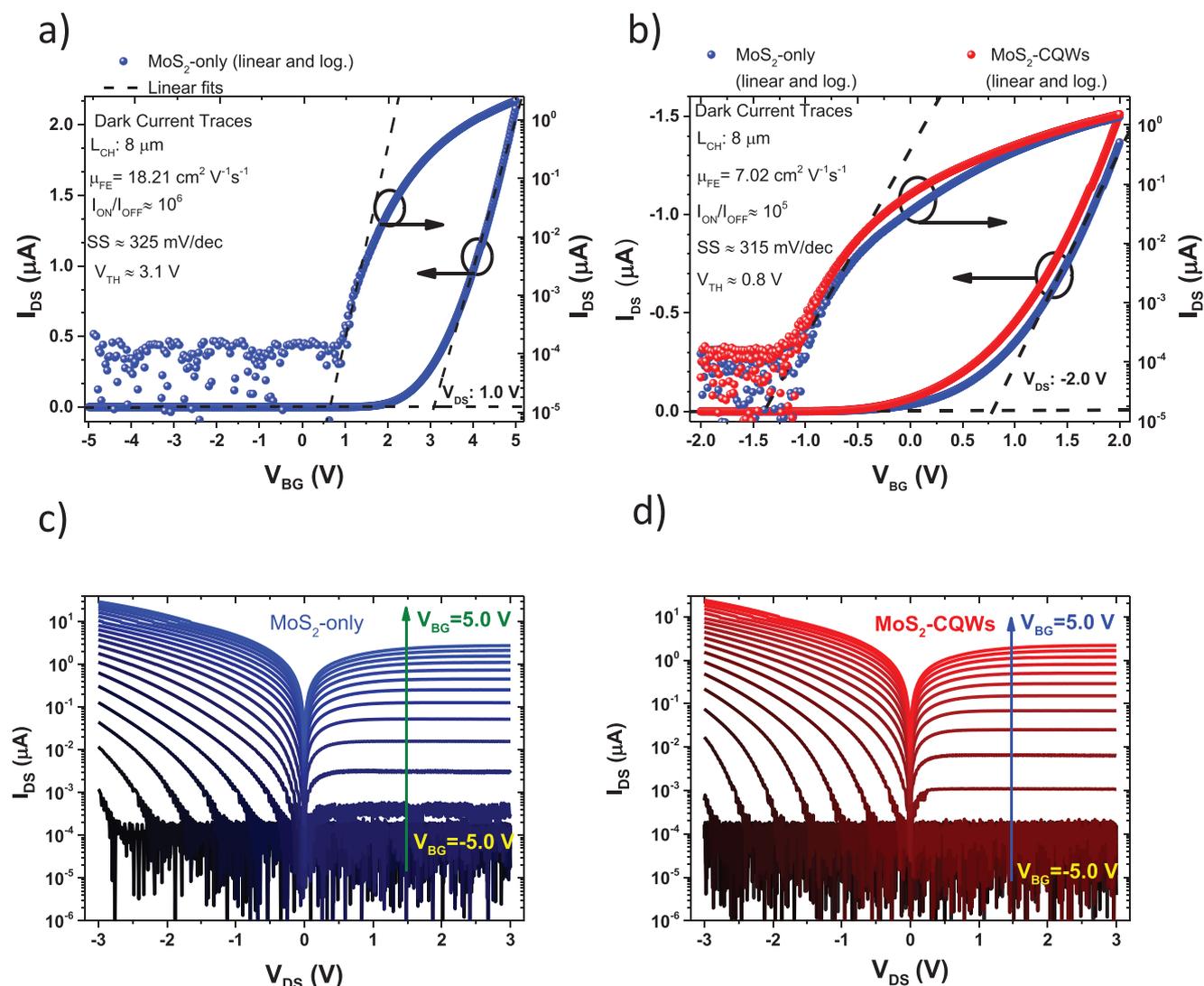
Figure 2. Electronic transport measurements of the pristine and hybrid devices under dark conditions. a) Transfer characteristics ($I_{DS} - V_{BG}$) of the MoS_2-only device at $VDS = 1.0$ V under dark conditions. b) The transfer characteristics of the MoS_2-only and MoS_2-CQWs devices at $V_{DS} = -2.0$ V under dark conditions. The output characteristics ($I_{DS} - V_{DS}$) of c) MoS_2-only and d) MoS_2-CQWs devices for V_{BG} sweep from -5.0 to 5.0 V under dark conditions.

of CQWs with a nonaromatic ligand of oleic acid and mixing dilution in hexane/PMMA, which is in consistent with previous experimental studies.[34] If the PL lifetime of CQWs (donor) in the absence of MoS_2 (acceptor) is τ_D, and the lifetime of CQWs on MoS_2 (donor–acceptor pair) is τ_{DA}, the FRET efficiency and rate can be estimated from $\eta_{FRET} = 1 - \left(\dfrac{\tau_{DA}}{\tau_D}\right)$ and $\Gamma_{FRET} = \dfrac{1}{\tau_{FRET}} = \dfrac{1}{\tau_{DA}} - \dfrac{1}{\tau_D}$, assuming that the donor lifetime modification is purely from FRET. Based on this estimation in our hybrid, we extracted a FRET efficiency level of 97.84% along with a fast FRET rate of 21.26 ns^{-1}, indicating an ultra-efficient transfer of excitons from the CQWs to the monolayer of MoS_2.

We also performed electrical measurements of our fabricated devices under ambient conditions at room temperature for both the dark and illuminated states. It is worth mentioning that Si substrate is used as the back-gate contact for the modulation of I_{DS} current. The dark current characteristics of the devices

are not only important for photocurrent extraction but also useful to reveal any electronic or physical modification on the device before and after introducing the CQWs layer. To this end, the transport measurements of the pristine and hybrid devices are presented in **Figure 2**. Figure 2a shows the transfer characteristics of the bare monolayer MoS_2 device on the logarithmic and linear scales with a positive bias of $V_{DS} = 1.0$ V. The back-gate voltage sweep range of the positively biased device is larger than the negatively biased one (Figure 2b) to observe the modulated maximum saturation current. This asymmetric bias characteristic of devices is due to the formation of asymmetric Schottky contacts between MoS_2 and Au/ Ti metal contacts. The asymmetric Schottky barrier is usually caused by fermi level pinning (FLP), the oxidation of metal contacts due to the adsorption at the metal-semiconductor interface and the difference between the work functions of channel and contact materials.[43] Furthermore, it has been shown that

ADVANCED
SCIENCE NEWS
www.advancedsciencenews.com

ADVANCED
OPTICAL
MATERIALS
www.advopticalmat.de

applying higher gate voltages results in an increase in the gate leakage currents which is not desired and suitable for the integrated circuits. The gate sweep range of the positively biased device is larger (−5 to 5 V) than the one (−2 to 2 V) biased with negative drain-source voltage to achieve similar maximum I_{DS} current. Therefore, to keep the gate leakage current at low levels, as to apply a narrow gate-voltage sweep range, all pristine and hybrid devices were biased with a negative bias of $V_{DS} = -2.00$ V. The transfer characteristics of the MoS$_2$-only and MoS$_2$-CQWs devices under dark conditions at $V_{DS} = -2.0$ V are depicted in Figure 2b in both logarithmic and linear scales. Here, threshold voltages (V_{TH}) are determined from the linear regime of the on-state conduction via a commonly used method of linear extrapolation (LE),[44] where the tangent line with a maximum slope on the transfer curve at the peak transconductance (g_m) is linearly extrapolated to extract V_{BG} axis crossing and V_{TH} value by adding $\frac{V_{DS}}{2}$ to this intercept at V_{BG} axis. The estimated threshold voltages for MoS$_2$-only and MoS$_2$-CQWs devices are −0.5 and −0.3 V, respectively. Here similar values of V_{TH} for MoS$_2$-only and MoS$_2$-CQWs indicate that there is no charge transfer from CQWs to MoS$_2$ which would otherwise be expected to change the V_{TH},[22] consistent with our previous systematic optical study on FRET from CQWs to MoS$_2$. In addition, as can be seen in Figure 2b, the dark currents for both cases follow very similar behavior which is another evidence supporting the absence of charge transfer or of doping effect in our hybrid system.

The field-effective carrier mobility (μ_{FE}), subthreshold swing value (SS) and the current ON/OFF ratio of the fabricated devices are used to reveal the electronic transport performances. The field-effect mobilities were estimated from the calculated transconductance $g_m = \frac{\partial I_{DS}}{\partial V_{BG}}$ using the following expression:

$$\mu_{FE} = \frac{L_{CH}}{W_{CH}} \frac{1}{V_{DS}C_g} \frac{\partial I_{DS}}{\partial V_{BG}} \quad (cm^2 \ V^{-1} \ s^{-1}) \tag{1}$$

where I_{DS} is the drain-source current, $\frac{L_{CH}}{W_{CH}}$ is the ratio of length to width of the channel, V_{DS} is the bias voltage and C_g is the gate capacitance per unit area. C_g can be defined as $C_g = \frac{\varepsilon_g}{t_g}$ where ε_g is the dielectric constant and t_g is the thickness of the gate oxide.[45] The calculated μ_{FE} values are 7.02 and 18. 21 cm^2 V^{-1} s^{-1} for the negatively and positively biased devices, respectively, which are rather high carrier mobilities for our device architecture and measurement conditions.[45] The fabricated devices provide a significantly high current ON/OFF ratio of ≈10^5 and very low SS values of 315 and 325 mV dec^{-1} under positive and negative biases, respectively. The characteristic curves (I_{DS}-V_{DS}) of the MoS$_2$-only and MoS$_2$-CQWs based devices are given in Figures 2c and 2d, respectively, for the gate modulation voltage swept from $V_{BG} = -5.0$ to 5.0 V with an interval of 0.5 V. To further examine effect of the sensitization layer (i.e., CQWs layer) on the output characteristics of the devices under dark condition, we swept V$_{DS}$ voltage from −3.0 to 3.0 V. Later, the maximum saturation currents (I_{DSS}) were measured before and after of the CQWs layer deposition and the measured values are found very close to each other, indicating that the CQWs layer does not cause any observable modification without illumination.

To evaluate the enhancement in optoelectronic performance of the sensitized MoS$_2$ phototransistor compared to the pristine MoS$_2$ one, we investigated the photocurrent-bias voltage (I_{PH}-V_{DS}) (**Figure 3**a) and the photocurrent-gate voltage ($I_{PH}-V_{BG}$) characteristics (Figure 3b). The photocurrent(I_{PH}) was quantified from the measured difference between the currents under illuminated and dark conditions ($I_{PH} = I_{LIGHT} - I_{DARK}$) for different values of V_{DS} and V_{BG}. Figure 3a represents $I_{PH} - V_{DS}$ curves of both pristine and sensitized MoS$_2$ phototransistor which are measured under the UV light of 375 nm and 1 mW for the back-gate voltages tuned from 2.0 to 5.0 V with an interval of 0.5 V. As expected, the photocurrents of both MoS$_2$-only and MoS$_2$-CQWs devices are increased with the rising illumination power. Owing to an efficient FRET process, the photocurrent of the MoS$_2$-CQWs device is dramatically enhanced with respect to the MoS$_2$-only one for all gate voltages (Figure 3a,b). The maximum photocurrent enhancement in the sensitized phototransistor was found to be threefold larger compared to the pristine MoS$_2$ device. Furthermore, by increasing the illumination power, I_{PH}-V_{BG} curves of both devices shifted in negative gate voltages which also indicates the threshold voltage shift (Figure 3b). The threshold voltages of the illuminated transfer curves extracted by LE method and the shift in the threshold voltages, which is the difference between the threshold voltages of the illuminated ($V_{TH(ILL)}$) and dark ($V_{TH(DRK)}$) measurements ($\Delta V_{TH} = V_{TH(ILL)} - V_{TH(DRK)}$) for both devices, are plotted in Figure 3c as a function of the incident power. The shift in the threshold voltages (ΔV_{TH}) is increased by increasing the incident illumination power, which can be considered as a signature of photogating, also commonly referred to as the photovoltaic effect. The MoS$_2$-CQWs device offers a smaller threshold voltage shift range compared to the MoS$_2$-only device, where ΔV_{TH} varies from ≈630 to ≈860 mV for the CQWs-MoS$_2$ and from ≈150 to ≈770 mV for the MoS$_2$-only. However, at a low level of illumination power (at 1 μW), ΔV_{TH} exhibits a higher absolute shift value of ≈630 mV compared to the absolute shift value (≈150 mV) of MoS$_2$-only device. This higher absolute shift value can be attributed to the effect of the energy transfer from CQWs to MoS$_2$ layer thanks to the increased exciton population in the MoS$_2$ layer. Moreover, $\Delta V_{TH} - P_{IL}$ curves of both devices are fitted well with the function of $\Delta V_{TH} = a P_{IL}^b$[46] where α and b are constants. Here, the obtained b values for the sensitized- and pristine-MoS$_2$ device is ≈ 0.45 and ≈0.07, respectively. Both b values are smaller than 1, confirming the illumination power dependent threshold voltage and the occurrence of photogating effect. Here, the shift in threshold voltage with respect to illumination power tends to saturate for both device structures with different accelerations, indicating the density of photogenerated carriers in active layers almost reaches its maximum revealing that the photogating effect in sensitized device is stronger than one in pristine due to higher b value. This is an expected result due to positive contribution of FRET on photogating. To further understand the mechanism under laying the photocurrent enhancement and the effect of FRET on MoS$_2$, the log-plotted photocurrent (I_{PH}) curves of the MoS$_2$-CQWs and MoS$_2$-only devices with respect to the illumination power were fitted by a linear function of $I_{PH} \propto P_{IL}^\alpha$, where the obtained α factor gives information about the rate of photogating and photoconductivity effects (Figure S3a,b, Supporting Information). The

ADVANCED
SCIENCE NEWS
www.advancedsciencenews.com

ADVANCED
OPTICAL
MATERIALS
www.advopticalmat.de
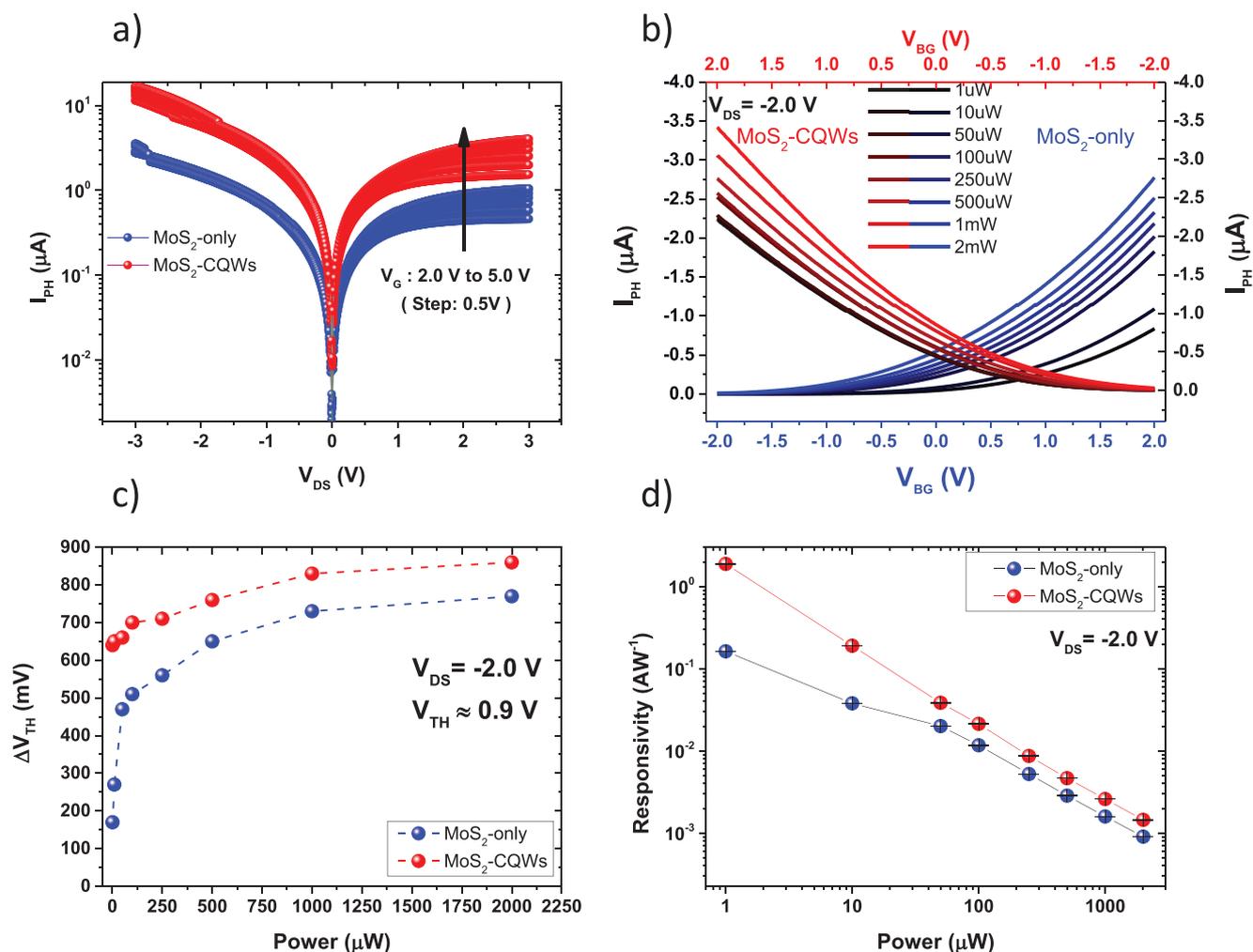
Figure 3. Optoelectronic performance of the CQWs-MoS$_2$ phototransistor compared to the bare MoS$_2$ phototransistor. a) I_{PH}–V_{DS} curves under illumination (P_{IL}) for a range of back-gate voltage (swept from 2.0 to 5.0 V) and b) the transfer characteristics of the photocurrent (I_{PH}–V_{BG}) as a function of the illumination power (from 1 to 2 mW) of the MoS$_2$-CQWs (red) and the MoS$_2$-only (blue) devices. c) Threshold voltage shift and d) photoresponsivity of both devices under the bias voltage of −2.0 V as function of the increasing illumination power.

photogating effect results in linear increase in the photocurrent as a function of the illumination power ($I_{PH} \propto P_{IL}$), while photoconductivity exhibits sublinear dependency on the incident power ($I_{PH} \propto P_{IL}^{\alpha}$ where $\alpha < 1$).[46–48] The fitting parameter of α is plotted as a function of the gate voltage for both devices in Figure S3c, Supporting Information. α declines from 1.00 (at $V_{BG} = -2.0$ V) to 0.14 (at $V_{BG} = 2.0$ V) for MoS$_2$-only device, indicating that the prevailing effect is purely photoconductivity at $V_{BG} = -2.0$ V but turning into photogating effect as the back-gate voltage increases from −2.0 to 2.0 V.

On the other hand, the α exponent decreases from 0.70 (at $V_{BG} = -2.0$ V) to 0.06 (at $V_{BG} = 2.0$ V) for the MoS$_2$-CQWs device, which shows that both of the mechanisms coexist at $V_{BG} = -2.0$ V and the photogating is the dominant mechanism at the elevated back-gate voltages. The photogating effect in the layered materials occurs due to the consequence of long-lived traps at the surface or interface, which are mainly induced during the growth process as S-vacancies.[41] The decrease in the α exponent for the MoS$_2$-CQWs device compared to the pristine MoS$_2$ device at all gate voltages suggest that the energy

transfer from the CQWs to the MoS$_2$ layer is also coupled by the traps states of MoS$_2$ and results in an increased effect of the photogating.

Additionally, we estimated the photoresponsivity of both devices from $R = \dfrac{I_{PH}}{P_{eff}}$ where $P_{eff} = P_{in} \times \dfrac{A_{device}}{A_{beamspot}}$, A is the area and I_{PH} is the photocurrent. The estimated R values are plotted as a function of the illumination power at $V_{BG} = 2.0$ V in Figure 3d. In particular, at 1 µW of illumination power, the maximum R of the MoS$_2$-only device is found to be ≈0.16 AW^{-1}, while for MoS$_2$-CQWs device, the maximum R is ≈1.88 AW^{-1}, which corresponds to ≈11-fold enhancement as a result of the ultra-efficient FRET from the CQWs to the MoS$_2$ layer enabling a substantially higher level of the photoresponsivity factor at the operating illumination power levels. Furthermore, the effect of the gate voltage on photoresponsivity is investigated by estimating the responsivity as a function of gate voltage and calculating the responsivity ratio of MoS$_2$-CQWs to MoS$_2$-only devices which are depicted in Figure S3d,e, Supporting Information. The effectiveness of the CQW sensitization layer

**ADVANCED
SCIENCE NEWS**
www.advancedsciencenews.com

**ADVANCED
OPTICAL
MATERIALS**
www.advopticalmat.de

is clearly visible from the gate dependent responsivity curve. The maximum photoresponsivity enhancement is achieved as $\approx 5 \times 10^2$ − fold at $V_{BG} = -1.5$ V under 1 µW laser excitation power and $V_{DS} = -2.0$ V. This performance enhancement is a result of almost two order of magnitude increased photocurrent due to the transferred energy from the CQWs to the MoS$_2$ layer. The temporal response of the MoS$_2$-only and the MoS$_2$-CQWs devices is shown in Figures S4a and S4b, Supporting Information, respectively. The decay and rise times of both devices are in the orders of seconds due to the trap states at the oxide material interface or surface adsorbates, fully consistent with the reported values in the literature.[21,49] The high surface-to-volume ratio of MoS$_2$ affects the optoelectronic performance of the MoS$_2$-based devices due to a large number of trap states and adsorbates in the air which causes persistent photocurrents and acts as recombination centers.[21,49] Therefore, large decay and rise times for MoS$_2$-only and MoS$_2$-CQWs devices is correlated to that interface effect. In addition, the speed performance of the hybrid device is shown to be degraded with respect to

the pristine one. The reason for this degradation is suggested to be related to the additional trap states that are formed at the interface of CQWs-MoS$_2$. The effects of illumination, back-gate voltage modulation, and FRET process on the channel current transport and energy band alignment are illustrated and explained in detail through the schematics of **Figure 4**. The work functions (∅) of MoS$_2$, Si, and Al$_2$O$_3$ are taken 4.23,[11,50] 4.10,[50] and 2.80–0.90 eV,[51] respectively. Because of the physical distance between, the CQWs and the MoS$_2$ (which is due to a nonaromatic ligand of oleic acid of CQWs and also possibly diluted PMMA host) the charge transfer is ineffective between the sensitizer layer and the MoS$_2$ monolayer. The channel current transfer is mainly modulated by the back-gate voltage. For $V_{BG} > V_{TH}$, there is a large drift current (Figure 4c,g,j). On the other hand, there is a small or no drift current for $V_{BG} < V_{TH}$ (Figure 4d,h,k). The addition of CQWs layer on top MoS$_2$ enhances the photo-induced current by highly efficient transfer of the excitation energy through an electromagnetic dipole-dipole coupling process (Figure 4j,k). Owing to FRET, the
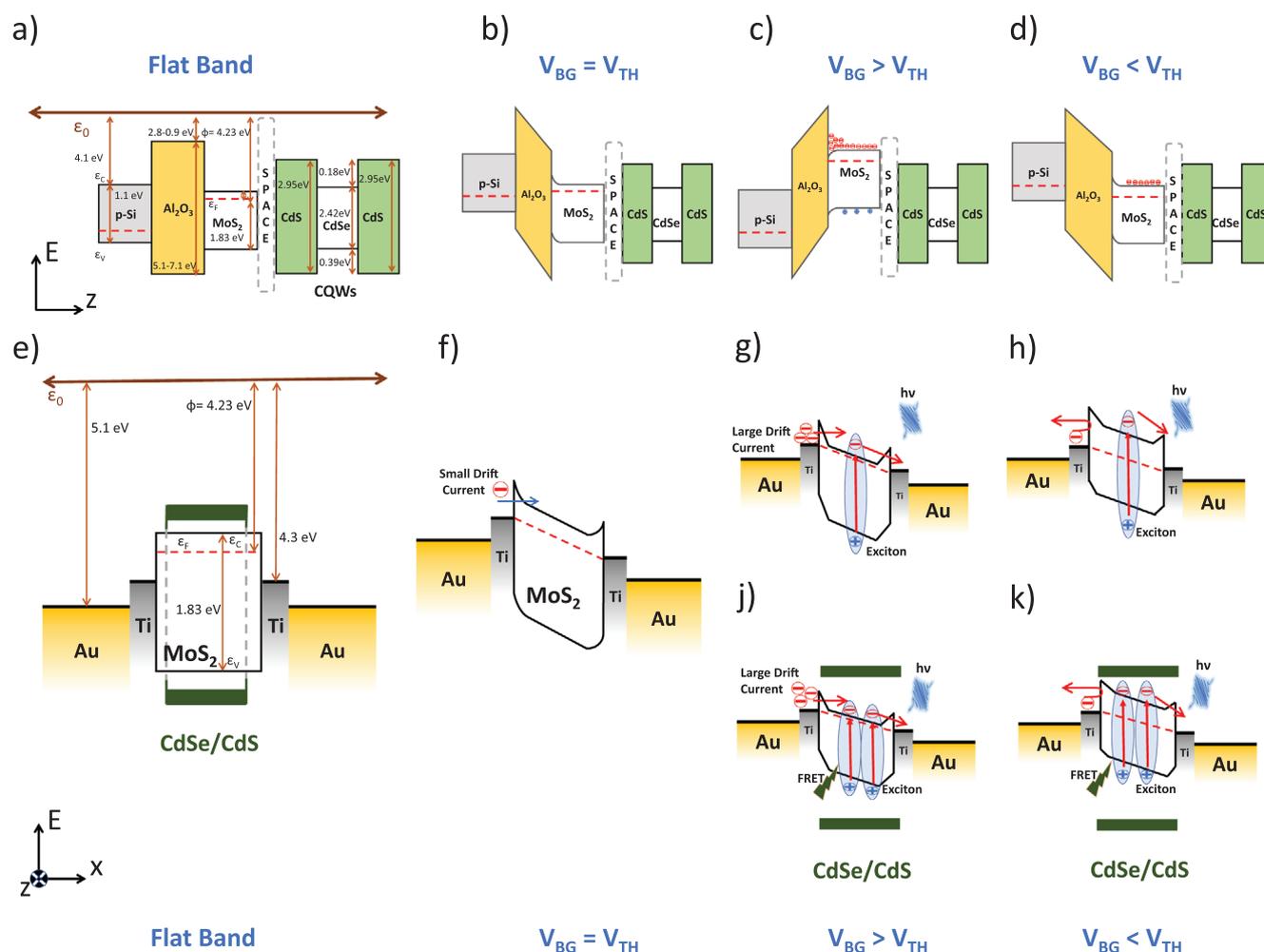
Figure 4. Schematics of channel current transport mechanism with and without the assistance of FRET process and energy band diagram of the MoS$_2$-CQWs and the MoS$_2$-only phototransistors: a,e) Flat band diagrams; b,f) under $V_{BG} = V_{TH}$; c) $V_{BG} > V_{TH}$ (ON-state), g) without CQWs and j) with CQWs; and d) $V_{BG} < V_{TH}$ (OFF-state), h) without CQWs and k) with CQWs. The schematics in (a)–(d) are in Ez plane without illumination and the schematics in (e)–(k) are in Ex plane with illumination but the band states of CQWs drawn in (g)–(k) are on Ez plane that show Ex plane just for the demonstration purposes. E stands for the energy-axis.

a)

b)
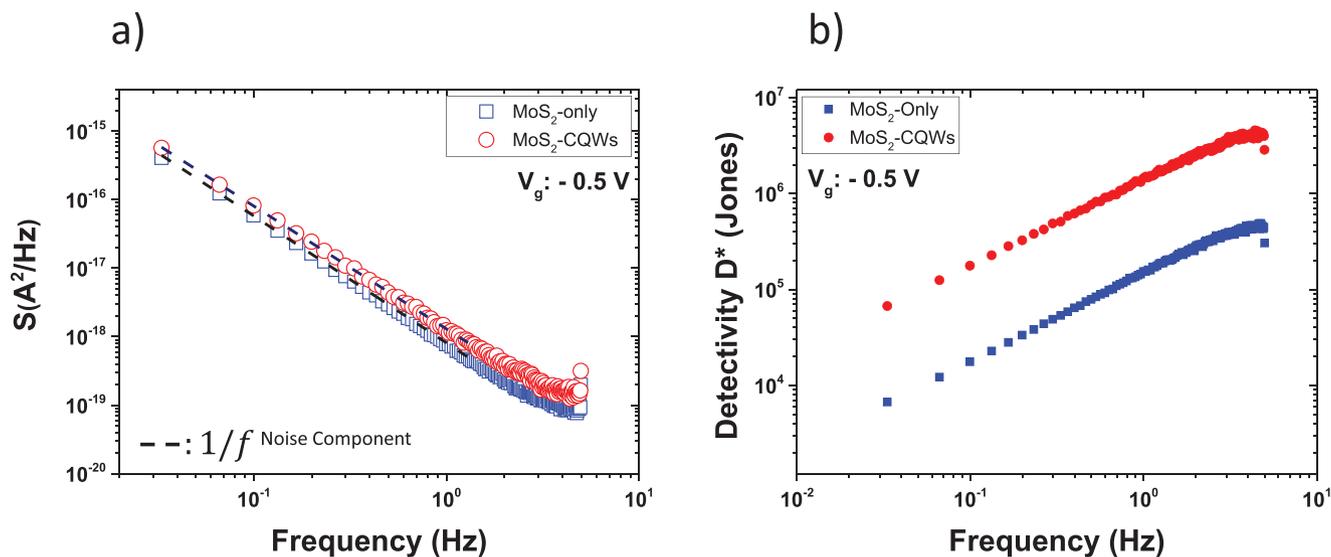
Figure 5. a) Noise power density and b) specific detectivity ($D*$) of the MoS$_2$-CQWs and MoS$_2$-only phototransistors operated at $V_{BG} = -0.5$ V and $VDS = -2.0$ V.

recombination lifetime of electron-hole pairs in MoS$_2$ is elongated, resulting in a larger photocurrent. The energy transfer process also increases the effectiveness of the photo-gating over the photoconductivity as discussed above.

Finally, we analyzed another important figure-of-merit for our phototransistors, the specific detectivity ($D*$) which can be defined as $D* = (AB)^{1/2}/\text{NEP} = RA^{1/2}/S_n$, where A is the active photodetection area, B is the noise bandwidth, NEP is the noise equivalent power, R is the responsivity, and S_n is the noise spectral density. To obtain the noise spectral density, dark current traces were measured at constant gate (V_{BG}) and bias (V_{DS}) voltages (under the same conditions that were used for the optical characterization) at a sample rate of 10 Hz. Then, the noise power density curves were calculated from fast Fourier transform of the dark current traces, which are shown in **Figure 5**a, where the noise power density of the sensitized and pristine MoS$_2$ devices are almost the same. Consequently, the noise power density curves of both devices were fitted with a linear function, for which both devices exhibit a similar noise behavior of $1/f$. This behavior is in good agreement with the previously reported 2D-MoS$_2$ based phototransistors and the noise power density rises as a function of $1/f$ due to the fluctuations in the mobility of the carriers.[52] The calculated $D*$ for the CQWs-MoS$_2$ and MoS$_2$-only devices are shown as a function of the frequency in Figure 5b. As shown in Figure 5b, thanks to the ultra-efficient ($\approx$98%) FRET from the layer of CQWs to that of MoS$_2$ in the hybrid MoS$_2$-CQWs device (red-colored data points), the estimated $D*$ is enhanced by tenfolds compared to the pristine MoS$_2$ device (blue-colored data points).

3. Conclusions

In conclusion, we have proposed and demonstrated a novel hybrid MoS$_2$-CQWs phototransistor where the CQWs acts as a layer of sensitization in our device architecture. Owing to the ultrafast ($\approx$21 ns^{-1}) and ultra-efficient FRET ($\approx$98%) from the

sensitization layer (CQWs) to active layer (MoS$_2$) in our device structure, we achieved a two order of magnitude enhancement in the photoresponsivity performance compared to pristine MoS$_2$ phototransistors. In addition, a tenfold enhancement was obtained in the specific detectivity of the sensitized device. Moreover, from the transport characteristics, we show that due to the assistance of FRET in our hybrid system, the contribution of the photogating mechanism is enhanced compared to the photoconductivity effect. The proposed hybrid device structure shown here using CQW sensitization offers a new pathway for hybrid 2D materials-based phototransistors with high performance levels, endorsing their use in optical communication, video imaging, and spectroscopy applications.

Supporting Information

Supporting Information is available from the Wiley Online Library or from the author.

Conflict of Interest

The authors declare no conflict of interest.

ADVANCED
SCIENCE NEWS

www.advancedsciencenews.com

ADVANCED
OPTICAL
MATERIALS

www.advopticalmat.de

[1] G. Eda, S. A. Maier, *ACS Nano* **2013**, *7*, 5660.

[2] V. K. Sangwan, M. C. Hersam, *Annu. Rev. Phys. Chem.* **2018**, *69*, 299.

[3] C. Xie, C. Mak, X. Tao, F. Yan, *Adv. Funct. Mater.* **2017**, *27*, 1603886.

[4] L. Yan, H. Shi, X. Sui, Z. Deng, L. Gao, *RSC Adv.* **2017**, *7*, 23573.

[5] E. Parzinger, B. Miller, B. Blaschke, J. A. Garrido, J. W. Ager, A. Holleitner, U. Wurstbauer, *ACS Nano* **2015**, *9*, 11302.

[6] Y. Li, A. Chernikov, X. Zhang, A. Rigosi, H. M. Hill, A. M. van der Zande, D. A. Chenet, E.-M. Shih, J. Hone, T. F. Heinz, *Phys. Rev. B* **2014**, *90*, 205422.

[7] M. Kang, B. Kim, S. H. Ryu, S. W. Jung, J. Kim, L. Moreschini, C. Jozwiak, E. Rotenberg, A. Bostwick, K. S. Kim, *Nano Lett.* **2017**, *17*, 1610.

[8] D. Lloyd, X. Liu, J. W. Christopher, L. Cantley, A. Wadehra, B. L. Kim, B. B. Goldberg, A. K. Swan, J. S. Bunch, *Nano Lett.* **2016**, *16*, 5836.

[9] N. Huo, S. Yang, Z. Wei, S.-S. Li, J.-B. Xia, J. Li, *Sci. Rep.* **2014**, *4*, 5209.

[10] Q. Zeng, Z. Liu, *Adv. Electron. Mater.* **2018**, *4*, 1700335.

[11] M.-L. Tsai, S.-H. Su, J.-K. Chang, D.-S. Tsai, C.-H. Chen, C.-I. Wu, L.-J. Li, L.-J. Chen, J.-H. He, *ACS Nano* **2014**, *8*, 8317.

[12] F. Xia, H. Wang, D. Xiao, M. Dubey, A. Ramasubramaniam, *Nat. Photonics* **2014**, *8*, 899.

[13] S. Ithurria, M. Tessier, B. Mahler, R. Lobo, B. Dubertret, A. L. Efros, *Nat. Mater.* **2011**, *10*, 936.

[14] M. D. Tessier, C. Javaux, I. Maksimovic, V. Loriette, B. Dubertret, *ACS Nano* **2012**, *6*, 6751.

[15] D. Dede, N. Taghipour, U. Quliyeva, M. Sak, Y. Kelestemur, K. Gungor, H. V. Demir, *Chem. Mater.* **2019**, *31*, 1818.

[16] N. Taghipour, S. Delikanli, S. Shendre, M. Sak, M. Li, F. Isik, I. Tanriover, B. Guzelturk, T. C. Sum, H. V. Demir, *Nat. Commun.* **2019**, *11*, 3305.

[17] B. Guzelturk, Y. Kelestemur, M. Olutas, S. Delikanli, H. V. Demir, *ACS Nano* **2014**, *8*, 6599.

[18] B. Liu, S. Delikanli, Y. Gao, D. Dede, K. Gungor, H. V. Demir, *Nano Energy* **2018**, *47*, 115.

[19] M. Sharma, K. Gungor, A. Yeltik, M. Olutas, B. Guzelturk, Y. Kelestemur, T. Erdem, S. Delikanli, J. R. McBride, H. V. Demir, *Adv. Mater.* **2017**, *29*, 1700821.

[20] N. Perea-López, Z. Lin, N. R. Pradhan, A. Iñiguez-Rábago, A. L. Elías, A. McCreary, J. Lou, P. M. Ajayan, H. Terrones, L. Balicas, *2D Mater.* **2014**, *1*, 011004.

[21] W. Zhang, J. K. Huang, C. H. Chen, Y. H. Chang, Y. J. Cheng, L. J. Li, *Adv. Mater.* **2013**, *25*, 3456.

[22] Y. Yang, N. Huo, J. Li, *J. Mater. Chem. C* **2017**, *5*, 11614.

[23] M. S. Choi, D. Qu, D. Lee, X. Liu, K. Watanabe, T. Taniguchi, W. J. Yoo, *ACS Nano* **2014**, *8*, 9332.

[24] S. H. Yu, Y. Lee, S. K. Jang, J. Kang, J. Jeon, C. Lee, J. Y. Lee, H. Kim, E. Hwang, S. Lee, *ACS Nano* **2014**, *8*, 8285.

[25] Y.-J. Hsiao, T.-H. Fang, L.-W. Ji, B.-Y. Yang, *Nanoscale Res. Lett.* **2015**, *10*, 443.

[26] L. Yu, Y. H. Lee, X. Ling, E. J. Santos, Y. C. Shin, Y. Lin, M. Dubey, E. Kaxiras, J. Kong, H. Wang, T. Palacios, *Nano Lett.* **2014**, *14*, 3055.

[27] W. Deng, Y. Chen, C. You, B. Liu, Y. Yang, G. Shen, S. Li, L. Sun, Y. Zhang, H. Yan, *Adv. Electron. Mater.* **2018**, *4*, 1800069.

[28] D. Kufer, I. Nikitskiy, T. Lasanta, G. Navickaite, F. H. Koppens, G. Konstantatos, *Adv. Mater.* **2015**, *27*, 176.

[29] D. Kufer, T. Lasanta, M. Bernechea, F. H. Koppens, G. Konstantatos, *ACS Photonics* **2016**, *3*, 1324.

[30] N. Huo, J. Kang, Z. Wei, S. S. Li, J. Li, S. H. Wei, *Adv. Funct. Mater.* **2014**, *24*, 7025.

[31] N. Huo, G. Konstantatos, *Nat. Commun.* **2017**, *8*, 572.

[32] W. Zhang, C.-P. Chuu, J.-K. Huang, C.-H. Chen, M.-L. Tsai, Y.-H. Chang, C.-T. Liang, Y.-Z. Chen, Y.-L. Chueh, J.-H. He, *Sci. Rep.* **2014**, *4*, 3826.

[33] W. J. Yu, Y. Liu, H. Zhou, A. Yin, Z. Li, Y. Huang, X. Duan, *Nat. Nanotechnol.* **2013**, *8*, 952.

[34] N. Taghipour, P. L. Hernandez Martinez, A. Ozden, M. Olutas, D. Dede, K. Gungor, O. Erdem, N. K. Perkgoz, H. V. Demir, *ACS Nano* **2018**, *12*, 8547.

[35] B. Guzelturk, H. V. Demir, *Adv. Funct. Mater.* **2016**, *26*, 8158.

[36] T. Forster, *Naturwissenschaften* **1946**, *33*, 166.

[37] M. Olutas, B. Guzelturk, Y. Kelestemur, K. Gungor, H. V. Demir, *Adv. Funct. Mater.* **2016**, *26*, 2891.

[38] J. Chen, X. Zhao, S. J. Tan, H. Xu, B. Wu, B. Liu, D. Fu, W. Fu, D. Geng, Y. Liu, W. Liu, W. Tang, L. Li, W. Zhou, T. C. Sum, K. P. Loh, *J. Am. Chem. Soc.* **2017**, *139*, 1073.

[39] H. Li, Q. Zhang, C. C. R. Yap, B. K. Tay, T. H. T. Edwin, A. Olivier, D. Baillargeat, *Adv. Funct. Mater.* **2012**, *22*, 1385.

[40] A. Özden, H. Şar, A. Yeltik, B. Madenoğlu, C. Sevik, F. Ay, N. K. Perkgöz, *Phys. Status Solidi RRL* **2016**, *10*, 792.

[41] H. Şar, A. Özden, İ. Demiroğlu, C. Sevik, N. K. Perkgoz, F. Ay, *Phys. Status Solidi RRL* **2019**, *13*, 1800687.

[42] S. Mouri, Y. Miyauchi, K. Matsuda, *Nano Lett.* **2013**, *13*, 5944.

[43] A. Di Bartolomeo, A. Grillo, F. Urban, L. Iemmo, F. Giubileo, G. Luongo, G. Amato, L. Croin, L. Sun, S. J. Liang, *Adv. Funct. Mater.* **2018**, *28*, 1800657.

[44] A. Ortiz-Conde, F. G. Sánchez, J. J. Liou, A. Cerdeira, M. Estrada, Y. Yue, *Microelectron. Reliab.* **2002**, *42*, 583.

[45] H. Şar, A. Özden, B. Yorulmaz, C. Sevik, N. K. Perkgoz, F. Ay, *J. Mater. Sci.: Mater. Electron.* **2018**, *29*, 8785.

[46] J. O. Island, S. I. Blanter, M. Buscema, H. S. van der Zant, A. Castellanos-Gomez, *Nano Lett.* **2015**, *15*, 7853.

[47] H. Wu, Z. Kang, Z. Zhang, Z. Zhang, H. Si, Q. Liao, S. Zhang, J. Wu, X. Zhang, Y. Zhang, *Adv. Funct. Mater.* **2018**, *28*, 1802015.

[48] L. Li, W. Wang, Y. Chai, H. Li, M. Tian, T. Zhai, *Adv. Funct. Mater.* **2017**, *27*, 1701011.

[49] O. Lopez-Sanchez, D. Lembke, M. Kayci, A. Radenovic, A. Kis, *Nat. Nanotechnol.* **2013**, *8*, 497.

[50] H.-M. Li, D.-Y. Lee, M. S. Choi, D. Qu, X. Liu, C.-H. Ra, W. J. Yoo, *Sci. Rep.* **2014**, *4*, 4041.

[51] S. K. Pradhan, B. Xiao, A. K. Pradhan, *J. Appl. Phys.* **2016**, *120*, 125305.

[52] V. K. Sangwan, H. N. Arnold, D. Jariwala, T. J. Marks, L. J. Lauhon, M. C. Hersam, *Nano Lett.* **2013**, *13*, 4351.